Editors' Suggestion

Stacking tunable interlayer magnetism in bilayer CrI_3

Peiheng Jiang,[1,*] Cong Wang,[2,*] Dachuan Chen,[1] Zhicheng Zhong,[1,3,†] Zhe Yuan,[4] Zhong-Yi Lu,[2] and Wei Ji[2,†]

[1]*Key Laboratory of Magnetic Materials and Devices & Zhejiang Province Key Laboratory of Magnetic Materials and Application Technology, Ningbo Institute of Materials Technology and Engineering, Chinese Academy of Sciences, Ningbo 315201, P.R. China*

[2]*Beijing Key Laboratory of Optoelectronic Functional Materials & Micro-Nano Devices, Department of Physics, Renmin University of China, Beijing 100872, P.R. China*

[3]*China Center of Materials Science and Optoelectronics Engineering, University of Chinese Academy of Sciences, Beijing 100049, P.R. China*

[4]*The Center for Advanced Quantum Studies and Department of Physics, Beijing Normal University, Beijing 100875, P.R. China*

(Received 10 July 2018; revised manuscript received 13 March 2019; published 1 April 2019)

Diverse interlayer tunability of physical properties of two-dimensional layers mostly lies in the covalent-like quasibonding that is significant in electronic structures but rather weak for energetics. Such characteristics result in various stacking orders that are energetically comparable but may significantly differ in terms of electronic structures, e.g., magnetism. Inspired by several recent experiments showing interlayer antiferromagnetically coupled CrI_3 bilayers, we carried out first-principles calculations for CrI_3 bilayers. We found that the antiferromagnetic coupling results from a different stacking order with the $C2/m$ space group symmetry, rather than the graphene-like one with $R\bar{3}$ as previously believed. Moreover, we demonstrated that the intra- and interlayer couplings in CrI_3 bilayer are governed by two different mechanisms, namely ferromagnetic superexchange and direct-exchange interactions, which are largely decoupled because of their significant difference in strength at the strong- and weak-interaction limits. This allows the much weaker interlayer magnetic coupling to be more feasibly tuned by stacking orders solely. Given the fact that interlayer magnetic properties can be altered by changing crystal structure with different stacking orders, our work opens a paradigm for tuning interlayer magnetic properties with the freedom of stacking order in two-dimensional layered materials.

DOI: 10.1103/PhysRevB.99.144401

I. INTRODUCTION

Magnetism in two dimensions has received growing attention since the two ferromagnetic mono- or bilayers, namely CrI_3 [1] and $Cr_2Ge_2Te_6$ [2], were successfully fabricated in 2017. The ferromagnetism in these two layers was believed to be stabilized by magnetic anisotropy as enhanced by spin-orbit coupling or external magnetic fields. Their Curie temperatures were up to ∼50 K. Very recently, a room-temperature T_c were achieved in monolayer VSe_2 [3] and $MnSe_x$ [4], two members of the transition-metal dichalcogenides family. This shed considerable light on the search for high T_c ferromagnetic (FM) magnets. However, the tunability of magnetism has been emerging as a new challenge. The coupling strengths of two-dimensional (2D) materials are significantly different between intra- and interlayer interactions. Such difference may offer diverse magnetic coupling mechanisms at strong and weak interacting limits. The interlayer magnetic coupling is of peculiar interest, as the effective coupling is relatively weak and confined within few atomic layers, which is much easier to model and more feasible to tune than strong and periodic couplings in three-dimension.

Recent experiments demonstrated that the antiferromagnetic (AFM) interlayer order in bilayer CrI_3 can be manipulated to a FM order by electric gating or reasonably large magnetic fields [5–12]. As a consequence, a magnetic tunnel junction with giant tunneling magnetoresistance values was achieved in bilayer CrI_3 devices [5–8]. These experimental demonstrations may open a new avenue for "interlayer" spintronics in magnetic bilayers. There are a few conjectures for the mechanism of the magnetic tunability, however, these arguments lack compelling support, and the details of the stacking geometry and the magnetic ground state are yet to be addressed [11]. The tunability also strongly relies on the initial geometry and the associated magnetic ground state of the bilayers, from which external fields change the magnetism. The interlayer stacking order was manifested as an effective and sustained way for tailoring geometry and the accompanying properties of bilayers, e.g., five times reduced shear force constants [13] and emerged strong correlation of electrons [14] in twisted graphene, unusual optical signals in folded MoS_2 [15], and a band tail state observed in simple-sliding $MoSe_2$ bilayers [16]. In light of this, it seems paramount to unveil the ground state stacking order and its roles in varying interlayer magnetic couplings and in selecting magnetic ground state of CrI_3 bilayers.

Here, we carried out first-principles calculations to unveil the stacking-dependent interlayer electronic and magnetic couplings in the CrI_3 bilayer. The intralayer FM of CrI_3 was ascribed to a Cr-I-Cr FM superexchange in which the Cr-I-Cr bond angle approaches 90° [17]. As a result of the Hund correlation effect, the magnetic moments of the both Cr atoms align parallel, which is rather robust under external perturbations. In terms of interlayer magnetism, a simple sliding of one layer of the bilayer could change the direct

*These authors contributed equally to this work.

†Authors to whom correspondence should be addressed: zhong@nimte.ac.cn; wji@ruc.edu.cn

hopping strength between interlayer I orbitals, which varies the interlayer magnetic ground state of the bilayer between interlayer FM and AFM ones. The AFM ground state allows the magnetic field to control the tunnel magnetoresistance effect, which was realized in the stacking tuned AFM coupled CrI_3 bilayer.

II. COMPUTATIONAL DETAILS

Our density functional theory calculations were performed using the generalized gradient approximation and the projector augmented wave method [18] as implemented in the Vienna *ab initio* simulation package (VASP) [19]. The uniform Monkhorst-Pack **k** mesh of $15 \times 15 \times 1$ was adopted for integration over the Brillouin zone (BZ). A plane-wave cutoff energy of 700 eV was used during the structural relaxations. A sufficiently larger distance of $c > 15$ Å along the out-of-plane direction was adopted to eliminate interaction between each layer. Dispersion correction with the optB86b functional [20] was adopted for structure related calculations, which was proved to be accurate in describing the structural properties of layered materials. For energy comparisons among different magnetic configurations, we used the Perdew-Burke-Ernzerhof (PBE) [21] and Heyd–Scuseria–Ernzerhof (HSE) [22,23] functionals, with the inclusion of spin-orbit coupling (SOC), based on the van der Waals–density functional (vdW–DF) revealed structures. Other functionals and vdWs have also been checked. On-site Coulomb interaction to the Cr d orbitals was self-consistently calculated based on a linear response method [24]. This calculation gives $U = 3.9$ eV and $J = 1.1$ eV, which were used in our calculations. The U-dependent calculations have also been done.

III. RESULTS AND DISCUSSIONS

Bulk CrI_3 exhibits a vdW structure and possesses a rhombohedral structure with the $R\bar{3}$ space group symmetry at low temperature (the LT phase). When temperature increases to 210–220 K, it undergoes a structural phase transition to a monoclinic lattice with the $C2/m$ space group symmetry (the HT phase) [25]. It is expected that a bilayer CrI_3 has similar structures to its bulk counterpart, namely, rhombohedral and monoclinic structures for low- and high-temperature exfoliated CrI_3 bilayers, respectively.

TABLE I. The lattice constants a and interlayer distance d of CrI_3 bilayer in different phases (LT and HT) and spin configurations (FM and AFM).

Configuration	a (Å)	d (Å)
LT-FM	6.92	3.48
LT-AFM	6.92	3.49
HT-FM	6.92	3.44
HT-AFM	6.92	3.46

The structural difference between these two phases of CrI_3 bilayers can be viewed as different stacking orders of single CrI_3 layers. In the LT phase, the stacking order is in analog to an *AB*-stacked graphene or a 2H-phase MoS_2 bilayer, in which a Cr atom of the bottom layer sits below the hollow site of the Cr hexagon as shown in Fig. 1(a). For the HT phase [Fig. 1(b)], it can be viewed as sliding the upper layer from the previous LT position with vector $\vec{s}$ (or $a/3$ along the zigzag direction, while a is the lattice constant) as indicated in Fig. 1(c). The lattice constants of both LT and HT phases with FM and AFM configurations were optimized and explicated shown in Table I. They show little difference with different phase and magnetic configuration, while the layer distances differ slightly, which should be contributed by the different stacking orders.

Total energy calculations with the inclusion of SOC show that the LT phase is more stable, and its energy is roughly 2.3 meV/Cr lower than that of the metastable HT phase. We further calculate the transition pathways from the LT to the HT phase in either interlayer FM or AFM coupled configuration as shown in Fig. 1(c). This indicates a transition barrier of

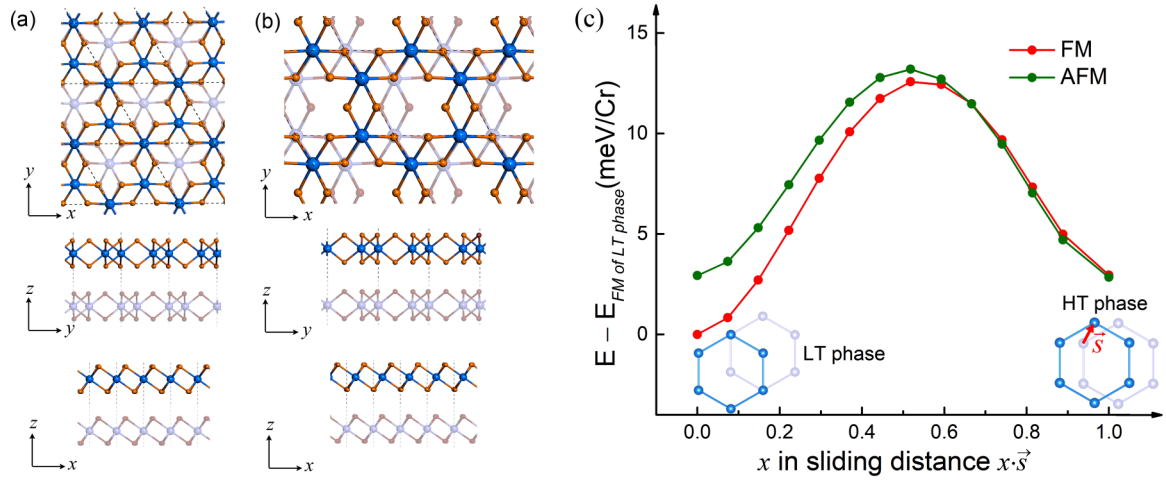

FIG. 1. (a), (b) Top and side views of the CrI_3 bilayer in the LT (a) and HT (b) phases. Slate-blue and dodger-blue balls represent Cr atoms and orange and maroon balls for I atoms. (c) Transition pathways between the two phases in FM and AFM configurations. The insets schematically illustrate LT and HT phases, indicating how interlayer structure changes during the transition between these two phases. The z axis of every atom in all structural optimizations have been fully relaxed. Spin-orbit coupling was not included for plotting panel (c).

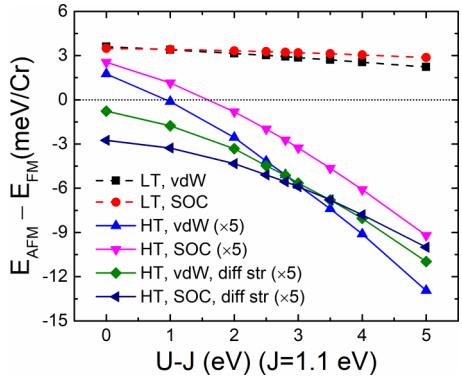

FIG. 2. Energy differences between AFM and FM states ($E_{\mathrm{AFM}} - E_{\mathrm{FM}}$) under different on-site Coulomb $U - J$ (J was fixed to 1.1 eV) values for the LT and HT phases. The vdW and SOC denote the calculation approaches with PBE + vdW and PBE + SOC, respectively. The calculations of FM and AFM configurations with different structures (see Appendix A) were donated as "diff str". The energy differences of HT phase have been enlarged five times.

roughly 10 meV/Cr, which may prevent the metastable HT phase transferring to the LT phase in the CrI_3 bilayer.

The magnetic ground state plays an important role in determining physical properties of materials. Experimentally, CrI_3 monolayer has a very strong intralayer FM order that persists up to ∼50 K [1]. Consistently, in our calculation, the FM state is at least 12 meV/Cr more favored than other magnetic configurations. Given this highly stable intralayer FM ground state, we next considered the interlayer magnetic couplings of the CrI_3 bilayer by comparing its energies with interlayer FM and AFM configurations. It is exceptional that the interlayer FM state is 3.23 meV/Cr more stable than the interlayer AFM state in the LT phase. Other functionals and vdW calculations also give similar results (see Appendix A). Such an energy difference in the LT phase is less influenced under different on-site Coulomb U values as shown in Fig. 2, hence the interlayer FM ground state for the LT phase is always maintained under different U values.

In terms of the HT phase, however, the interlayer magnetic ground state is an AFM one [7] with an energy difference ($E_{\mathrm{AFM}} - E_{\mathrm{FM}}$) of −0.54 meV/Cr. This result is valid under different functionals and vdWs (see Appendix A). Given this DFT + U scheme, we also check the calculations with different U values. As shown in Fig. 2, for the HT phase, the interlayer AFM coupling is more stable than the FM coupling when $U - J(J = 1.1$ eV) is larger than 1.0 eV for the PBE + vdW approach and 1.5 eV for the PBE + SOC approach. We should mention that the energies of different magnetic configurations ($E_{\mathrm{AFM}} - E_{\mathrm{FM}}$) discussed here are calculated using the same bilayer atomic structure (see discussion in Appendix B). When different atomic structures of FM and AFM are adopted (see Appendix B), as shown in Fig. 2, for either the PBE + vdW or PBE + SOC approach, the AFM state of the HT phase is more stable than the FM state no matter which value of U is adopted. These calculations verify the robustness of our calculated AFM ground state in the HT phase.

The small energy difference ($E_{\mathrm{AFM}} - E_{\mathrm{FM}}$) of −0.54 meV/Cr for the HT phase implies the interlayer spin-exchange coupling is rather weak ($J \sim 0.5$ meV), although the intralayer magnetic coupling was found to be much stronger ($J \sim 3$ meV). The weak interlayer magnetic coupling is consistent with the facts that the bandgap of the bilayer varies less than 0.15 eV from that of a CrI_3 monolayer [26], and that the cohesive energy of the bilayer is relatively small with a value of 14 meV/Å^2. Such a weak magnetic coupling in the HT phase indicates that the manipulation of its interlayer magnetism is, most likely, feasible by applying an external magnetic field.

These results of the LT and HT phases suggest that the interlayer AFM coupled CrI_3 bilayer [5,6,8–12], could, most likely, be maintained in the HT phase, rather than the presumed LT phase, even at low temperatures. This is, we believe, ascribed to structural quenching under rapid cooling rates and/or vertical confinement from the capping layers in the measurements, which could be directly verified by control experiments with slow cooling rates and removed capping layers.

We additionally examined the responses of the both phases to doping, electric field, and strain as shown in Fig. 3 and Appendix C. For the LT phase, the energy difference ($E_{\mathrm{AFM}} - E_{\mathrm{FM}}$) has a slightly quantitative dependence to doping, external electric field or strain. In other words, the FM ground state of the LT phase is so robust that it is unlikely to be tuned to the interlayer AFM configuration via these methods. For the HT phase, however, electron doping significantly changes the energy difference ($E_{\mathrm{AFM}} - E_{\mathrm{FM}}$), while hole doping nearly keeps the difference unchanged. More importantly, its magnetic configuration switches from the interlayer AFM ($E_{\mathrm{AFM}} - E_{\mathrm{FM}} < 0$) to FM ($E_{\mathrm{AFM}} - E_{\mathrm{FM}} > 0$) configuration when the doping concentration reaches 0.04 e/u.c., as shown in Fig. 3(c).

When an electric field is applied in the HT phase, the energy difference ($E_{\mathrm{AFM}} - E_{\mathrm{FM}}$) changes quite slightly, therefore the ground state of AFM is maintained. However, the total magnetization of its AFM ground state slightly increases as shown in Appendix D. This should be result from (i) charge transfer between two layers under electric field and (ii) the converse magnetization direction of each layer. However, the total magnetization of the FM configuration of the HT phase (can be realized by doping) is less influenced under electric field since the magnetization direction of each layer is exactly same. These theoretical calculations are consistent with the experimental discoveries in Ref. [11] and thus verify the solidness of our calculations.

We further extended our calculations to CrI_3 tri- and quadlayers to investigate whether the interlayer AFM order also maintains in CrI_3 multilayers. The interlayer AFM state still holds in all the considered HT multilayers and its bulk counterpart as shown in Fig. 4, which fully coincide with the recent experimental results [5,6]. This consistency strongly supports that the CrI_3 multilayers measured in the experiments still maintain the HT phase even at low temperature. In terms of the LT multilayers and the bulk form, the FM state is always the interlayer magnetic ground state.

Given the established magnetic ground state, we carefully examined the stacking difference resulting from variation of interlayer magnetic couplings in the CrI_3 bilayer. Figure 5(a)

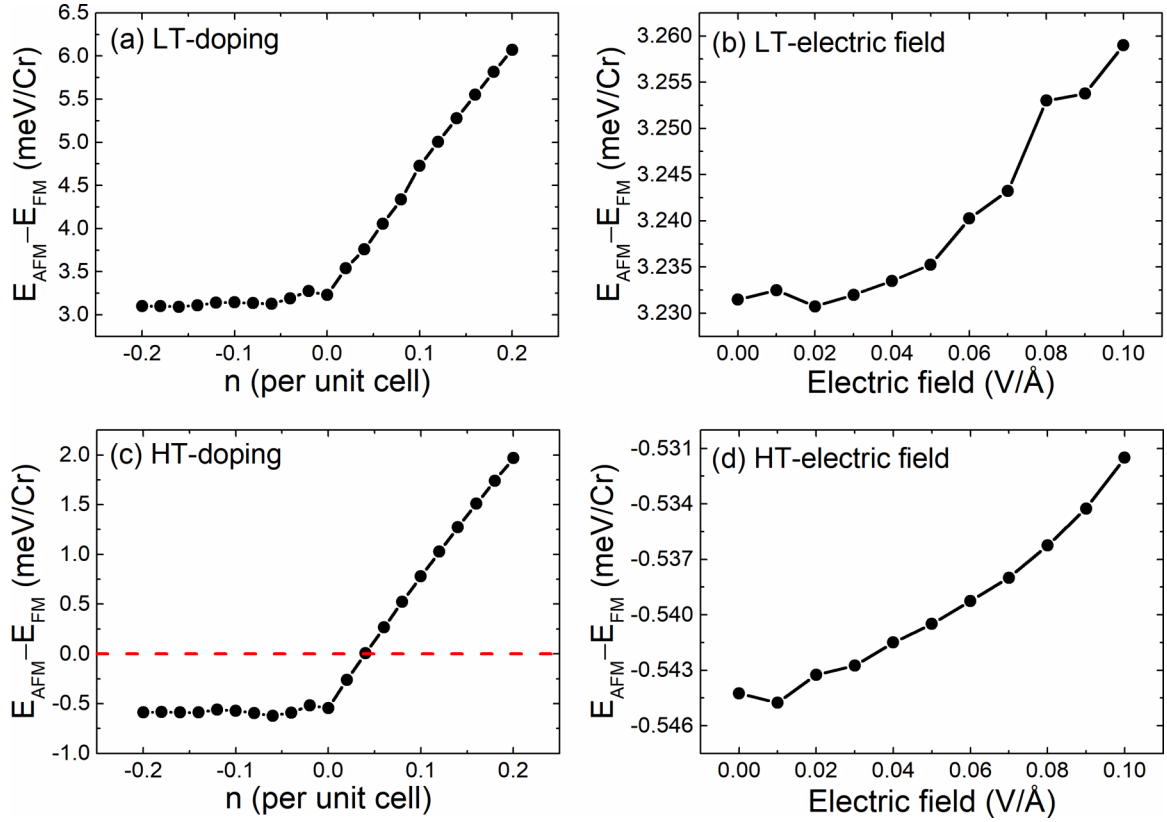

FIG. 3. Energy differences between AFM and FM states ($E_{\mathrm{AFM}}-E_{\mathrm{FM}}$) for the LT phase and HT phase under doping and electric field. The SOC has been considered here.

shows the charge accumulation at the interlayer region after stacking two CrI_3 layers together in the LT phase. Here, the amount of redistributed charge is comparable with that previously found in MoS_2 [27]. The accumulated charge mainly resides between close-contacted (4.20 Å) interlayer I-I pairs.

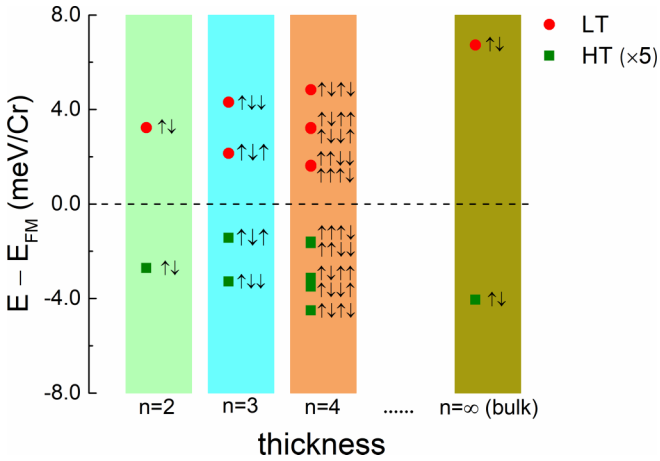

FIG. 4. Energy of different interlayer magnetic orders for bilayer ($n = 2$), trilayer ($n = 3$), quadlayer ($n = 4$), and bulk ($n = \infty$) CrI_3. The symbol ↑ and ↓ represent spin-up and spin-down, respectively. All energies have subtracted the energies of ferromagnetic (FM) states. The red and olive dots represent the energy of LT and HT phases, respectively. The energy of HT phase has been enlarged five times in order to show clearly. Here, the SOC has been considered.

The red arrow indicates an I-I pair that shares an appreciable amount of electrons, which bridges the interlayer magnetic coupling as we elucidated below.

In particular, the intralayer FM coupling is through a FM Cr-I-Cr superexchange, in which the Cr-I-Cr bond angle (93°) approaches 90° [17]. Here, we defined the two orbitals involved in the intralayer superexchange as p_{x} and p_{y}. As shown in Appendix Fig. 9, both Cr (3.28 μ_{B}) and I ($-0.12\,\mu_{\mathrm{B}}$) have local magnetic moments and the moments are in opposite directions, suggesting the spins of electrons of I atoms are polarized by Cr atoms. Local geometry shows that each I atom of the marked interlayer I-I pair has a $p_{\mathrm{x/y}}$ orbital interacting with the other one. Both orbitals are in a nearly linear configuration (an angle of 160°), indicating that the interaction is not owing to a FM superexchange. However, the shared electron indicates direct hybridization between the two $p_{\mathrm{x/y}}$ orbitals, leading to a direct FM coupling between the spin-down components (green) of the two I atoms. This mechanism is supported by the charge reduction around the $p_{\mathrm{x/y}}$ orbitals and the charge accumulation at the interlayer region in the spin-dependent differential charge density (DCD) of the spin-down component, as shown in Fig. 9. The FM coupled interlayer I atoms thus give rise to FM coupled interlayer Cr atoms through the intralayer Cr-I magnetic hybridization.

Here, both intralayer and interlayer Cr atoms are FM coupled, but are with different mechanisms. Both couplings are at the two extremes in terms of interacting strength, where the intralayer Cr-I-Cr superexchange sits at the strong-interaction limit, while the interlayer Cr-I …I-Cr direct exchange lies in

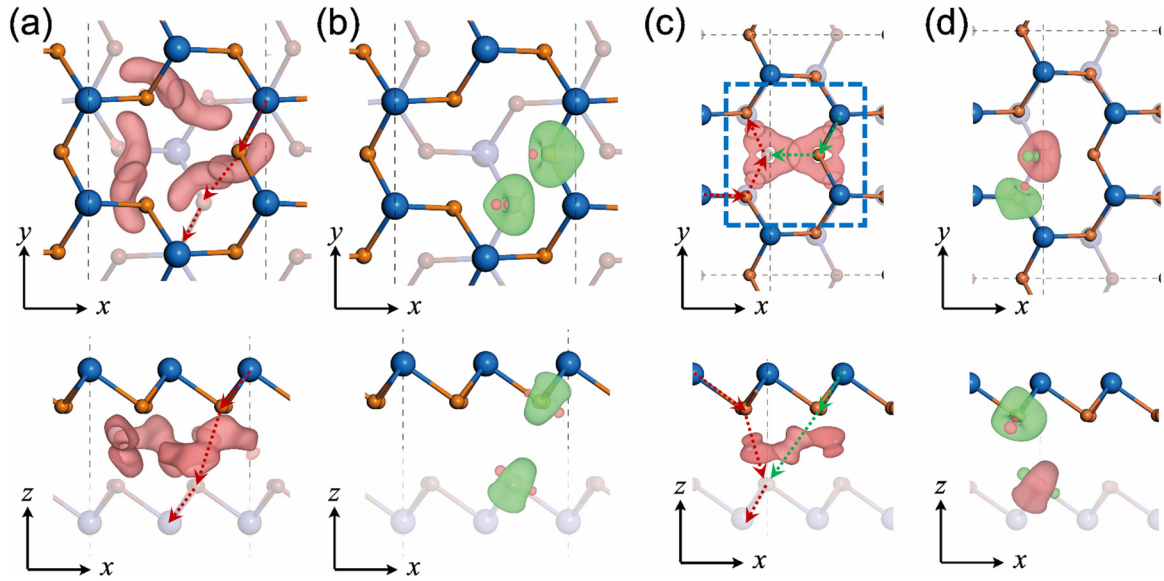

FIG. 5. Mechanism of interlayer magnetic couplings in LT and HT phases. (a) Differential charge density of the CrI_3 bilayer in the LT phase with both intra- and interlayer FM order (isosurface value of 0.0001 e/Bohr^3). Here, the light-rose isosurface contours show the charge accumulation after stacking those two layers together. Red dashed arrows indicate two interacting I atoms from the two CrI_3 layers. (b) Spin density of the two mentioned I atoms marked in (a). Red and green isosurface contours correspond to spin-up and -down charge densities, respectively. (c) Differential charge density of the CrI_3 bilayer in the HT phase with intralayer FM and interlayer AFM orders. The red and green dashed arrows, again, show the two interacting I atoms from both layers. (d) Spin density of the I atoms marked in (c). The SOC has been considered here.

the weak-interaction limit. Direct exchange couplings were usually found in metals, but in this case, it was found in a semiconductor with a nonmetal element. This exception is, most likely, due to strongly extended p wavefunctions of I and the vdW attraction induced overlap of interlayer $p_{x/y}$ orbitals. Although it is much weaker, the overlap is also a result of the known covalent-likely quasibond, as revealed in other 2D materials [27–31]. A similar but much stronger interlayer magnetic coupling ($J \sim 10$ meV) was found in CrS_2 bilayers [32], in which the bilayer strongly favors interlayer FM coupling and even changes an intralayer AFM order to the FM order. These results suggest that a much weaker interlayer coupling allows the interlayer magnetism to be more feasibly tuned.

Given the much weaker interlayer magnetic interaction of CrI_3, we thus expect the interlayer FM could be tuned to AFM through external perturbations. Given that a minor p_z spin density shows opposite sign to that of $p_{x/y}$ [Fig. 5(b)], a straightforward idea is to shift one layer of the bilayer, which favors direct exchange of a $p_{x/y}$ orbital from one layer with a p_z orbital from the other layer. The HT bilayer is just the case for this idea. Figure 5(c) shows the interlayer DCD of the HT bilayer. It shows the charge redistribution is slightly weaker than that of the LT bilayer and the charge accumulation mainly occurs around the six I atoms as marked in the blue dotted rectangular frame. In the HT case, electron sharing is not within a I-I pair, but through a tri-I cluster forming a triangle-shaped accumulated charge density. A red dashed arrow [Fig. 5(c)] marks two interlayer I atoms in the left triangle. The Cr-I…I-Cr interaction does not take a nearly linear configuration but is in a 135° configuration that a $p_{x/y}$ orbital of the top-layer I atom is oriented toward a p_z orbital of the bottom layer I atom with an interlayer I-I distance of 4.20 Å (red arrows). Direct charge transfer from the $p_{x/y}$ orbital to the p_z orbital is observable in the spin-dependent DCD (Fig. 9), indicating a direct $p_{x/y}$-p_z interaction. Here, the spin-orbit coupling may play a key role that the different parity symmetries of the $p_{x/y}$ and p_z orbitals do not obscure the hybridization. Since the $p_{x/y}$ orbital is spin polarized in the opposite direction to the p_z orbital, the direct $p_{x/y}$-p_z interaction results in an AFM coupling between interlayer I atoms. On the other hand, charge transfer between two triangles also gives rise to a $p_{x/y}$-$p_{x/y}$ interaction (green arrows) with a larger distance of 4.31 Å, making a weaker FM coupling compared with the former AFM one. Two competing Cr-I…I-Cr interactions, a stronger AFM $p_{x/y}$-p_z interaction and a weaker FM $p_{x/y}$-$p_{x/y}$ interaction, coexist in HT bilayer CrI_3, leading to the AFM coupled bilayer with a smaller FM/AFM energy difference.

The structural and magnetic differences of the LT and HT CrI_3 bilayers also result in different electronic band structures. Figure 6 shows the band structures of the LT and HT bilayers with both FM and AFM states (denoted as LT-FM, HT-FM, LT-AFM, and HT-AFM, respectively). It should be noted that the band structures of the two AFM states are double degenerate, while it is not the case for FM ones. For the LT bilayer, it exhibits the same stacking order with graphene bilayers where the hexagonal symmetry is maintained. The symmetry is, however, reduced in the HT bilayer because of the sliding of the upper layer. As a result, the six M/K points in the first BZ split into four M/K points and two M'/K' points.

The reduced symmetry leads to appreciable variations of band structures. The highest valence band (HVB) at the nonequivalent M' point is upshifted compared with the M point in either HT-FM or HT-AFM, resulting in the flatter

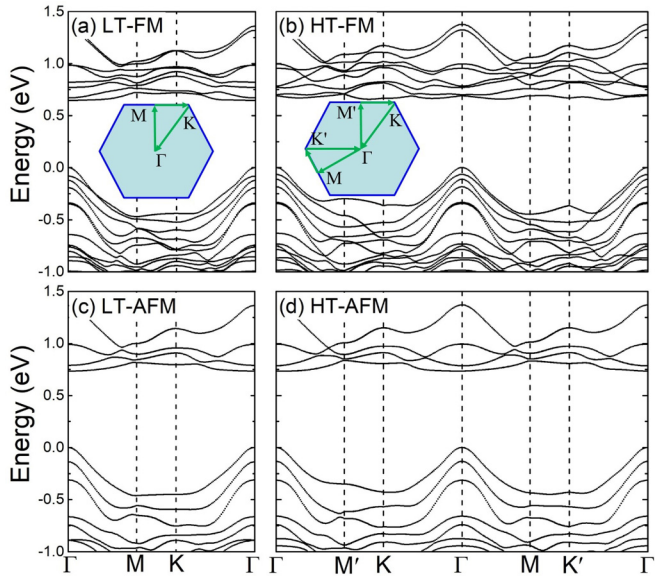

FIG. 6. Band structures of bilayer CrI_3. (a) LT phase with FM state; (b) HT phase with FM state; (c) LT phase with AFM state; (d) HT phase with AFM state. Spin-orbit coupling is included in all calculations. The insets are first BZs of two phases, which show the M' and K' are nonequivalent with M and K in the HT phase. The SOC has been considered here.

HVB of the HT bilayer than that of the LT bilayer. The PBE bandgaps of LT-FM, HT-FM, LT-AFM, and HT-AFM are 0.64, 0.66, 0.73, and 0.73 eV, respectively. All of them, except HT-FM, are direct bandgap semiconductors. The indirect bandgap of HT-FM results from a downshift of the lowest conductance band along M'-K. We thus expect diverse electronic band structures for LT-FM and HT-AFM because of the nonequivalent symmetry, different degenerate situations between the FM and AFM states, and variant bandgaps (differs about 90 meV) between them, as shown in Figs. 6(a) and 6(d).

IV. DISCUSSIONS AND CONCLUSIONS

In summary, we have carefully investigated the stacking orders of CrI_3 bilayers and successfully revealed stacking dependent magnetic couplings between the two CrI_3 layers. There are, at least, two stacking orders for CrI_3 bilayers, namely the HT and LT bilayers. Both bilayers take the FM intralayer magnetic order and the HT bilayer favors an AFM interlayer magnetic state. This AFM interlayer coupling is nearly decoupled from the intralayer FM coupling and the strength of it is largely reduced. In light of this, the interlayer magnetic configurations are changeable by a reasonably large external field, perturbations or change of local stacking geometry, while the intralayer FM state still maintains. Moreover, we should indicate that various stacking orders of CrI_3 bilayers will be experimentally accessible at low temperature, given the three experimentally realized stacking orderings of MoS_2 using well controlled fabrication conditions [33]. This offers an effective way to tune interlayer magnetic configuration in CrI_3 bilayers because of a locked stacking-magnetism coupling.

In previously revealed 3D magnetic materials, large magnetic moments and strong spin-exchange coupling are usually paramount for resisting thermal fluctuation, thereby achieving a high Curie temperature for practical applications. However, such large moments with strong spin-exchange couplings result in a significant amount of energy needed to manipulate the magnetic moments. Here, in 2D CrI_3 layers, the strong intralayer FM coupling keeps the magnetic moments ordered within each layer at finite temperature, yet the weak interlayer AFM coupling in the HT bilayer allows the magnetic moment of each layer to be feasibly manipulated. Given such close energies of the two couplings, we infer that magnetic domains with either FM or AFM interlayer coupling may be observable in a large area bilayer CrI_3 sample, which calls for subsequent experiments to verify. In addition, these two nearly decoupled magnetic couplings governed by two different mechanisms at the two interaction limits combines two apparently conflicting requirements of magnetic materials, which points to a new direction for seeking magnetic 2D layers in real applications. In addition, after being shown in tailoring mechanical, optical, and electrical properties, layer stacking was also illustrated in magnetic tunability.

ACKNOWLEDGMENTS

We thank Dr. Jiadong Zhou at Nanyang Technological University of Singapore for valuable discussions. We gratefully acknowledge financial support from the National Natural Science Foundation of China (Grants No. 11622437, No. 61674171, and No. 11774360), the Strategic Priority Research Program of Chinese Academy of Sciences (XDB30000000), the Fundamental Research Funds for the Central Universities, China, and the Research Funds of Renmin University of China (Grant No. 16XNLQ01). P.J. is supported by China Postdoctoral Science Foundation (Grant No. 2018M642497), and C.W. is supported by the Outstanding Innovative Talents Cultivation Funded Programs, 2017, of Renmin University of China. Calculations were performed at the Physics Lab of High-Performance Computing of Renmin University of China, Shanghai Supercomputer Center and the Supercomputing Center of Ningbo Institute of Materials Technology and Engineering.

TABLE II. Energy differences between interlayer AFM and FM states ($E_{AFM} - E_{FM}$) with consideration of different exchange functionals (including HSE hybrid functional). The spin-orbit coupling has been considered in all calculations except the HSE one.

$E_{AFM} - E_{FM}$ (meV/Cr)	PBE	PW91	LDA	revPBE	PBEsol	HSE
HT	− 0.544	− 0.815	− 0.823	− 0.554	− 0.698	− 2.295
LT	3.231	3.107	3.551	2.916	3.422	1.685

TABLE III. Energy differences between interlayer AFM and FM states ($E_{AFM} - E_{FM}$) with consideration of different vdWs. The spin-orbit coupling is not considered here.

		IVDW			VDW-DF			
$E_{AFM} - E_{FM}$ (meV/Cr)	No vdW	DFT-D2	DFT-D3	DFT-TS	revPBE	optPBE	optB88	optB86b
HT	− 0.908	− 0.908	− 0.908	− 0.906	− 1.040	− 1.036	− 1.151	− 1.018
LT	2.825	2.825	2.825	2.826	2.636	2.787	2.877	2.936

APPENDIX A: THE CALCULATED $E_{AFM} - E_{FM}$ WITH DIFFERENT FUNCTIONALS AND vdWs

The calculations in the main text are done within the PBE + SOC approach. To verify the reliability of our conclusion, we have done the calculation with different exchange functionals (including HSE) and different vdWs as shown in Tables II and III. All calculations indicate that for the HT phase, the AFM state is more stable than the FM state, and it is reversed for the LT phase. Therefore, our result is quite robust and will not be changed under a different functional.

APPENDIX B: STRUCTURES USED FOR ENERGY DIFFERENCE CALCULATIONS

We should indicate that, unless otherwise noted, all the calculations of FM and AFM states were done with the same structure, i.e., the one relaxed with the FM interlayer magnetic configuration. The reason should be that the energy difference between FM and AFM states is quite small, any difference in structure may lead to an energy difference comparable with it. In order to ensure that the energy difference comes from the magnetic configuration instead of structure, we adopt the same structure in both calculations of FM and AFM state.

We notice that such a setup favors FM couplings and may underestimate the preference of AFM couplings. Therefore, we also compare the AFM and FM energies using the structures fully relaxed in interlayer AFM and FM configurations, respectively. In other words, AFM energies with AFM relaxed structures and FM energies with FM relaxed structures. The calculated results have been shown in Fig. 2.

APPENDIX C: THE CALCULATED $E_{AFM} - E_{FM}$ UNDER DIFFERENT LAYER DISTANCES

We have calculated the energy differences between AFM and FM states ($E_{AFM} - E_{FM}$) under different layer distances for the HT and LT phases. The magnetic configurations of both the HT and LT phases CrI_3 bilayer will not be altered when the interlayer distance changes as shown in Fig. 7, which indicates the magnetic configurations are not sensitive to the uniaxial strain perpendicular to the xy plane. In addition, stacking of graphene or BN layers to the bilayer also varies the exact relative energy but does not change the order of stability of these two magnetic configurations.

APPENDIX D: THE TOTAL MAGNETIZATION UNDER ELECTRIC FIELD

When an electric field is applied in the HT phase, the total magnetization of its AFM ground state increases slightly, while that of the FM configuration is less influenced as shown in Fig. 8. In Ref. [11], it was concluded that "in the AFM phase, the electric field E induces a constant magnetization that increases with E'', and "in the FM phase, M_0 is nearly independent of E''. All these statements are consistent with our theoretical calculations and thus verify the solidness of our conclusions. Please note our calculated variation of the

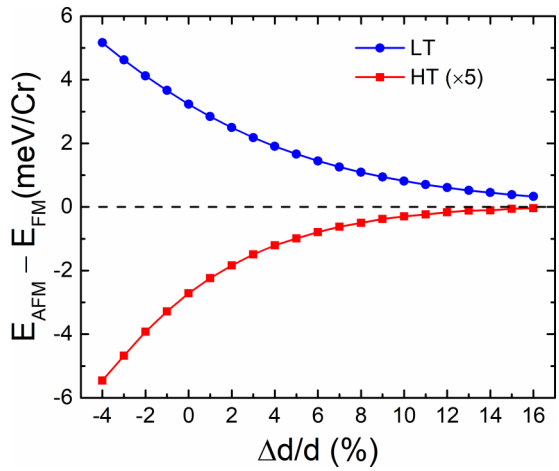

FIG. 7. Energy differences between AFM and FM states ($E_{AFM} - E_{FM}$) under different layer distances for the HT and LT phases. The energy differences of the HT phase are enlarged five times. The SOC has been considered here.

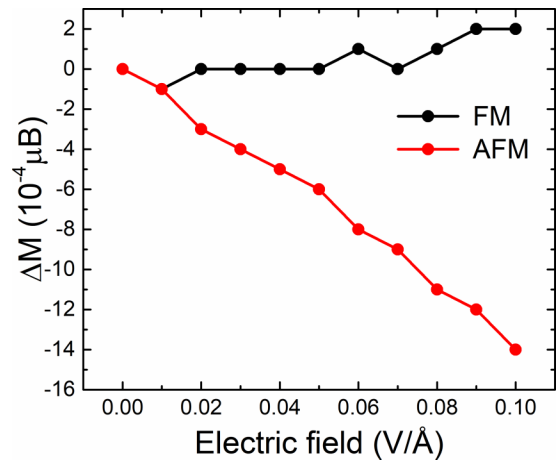

FIG. 8. Relative changes of total magnetization (four Cr atoms included) of both FM and AFM configurations in the HT phase as a function of electric field. The SOC has been considered here.

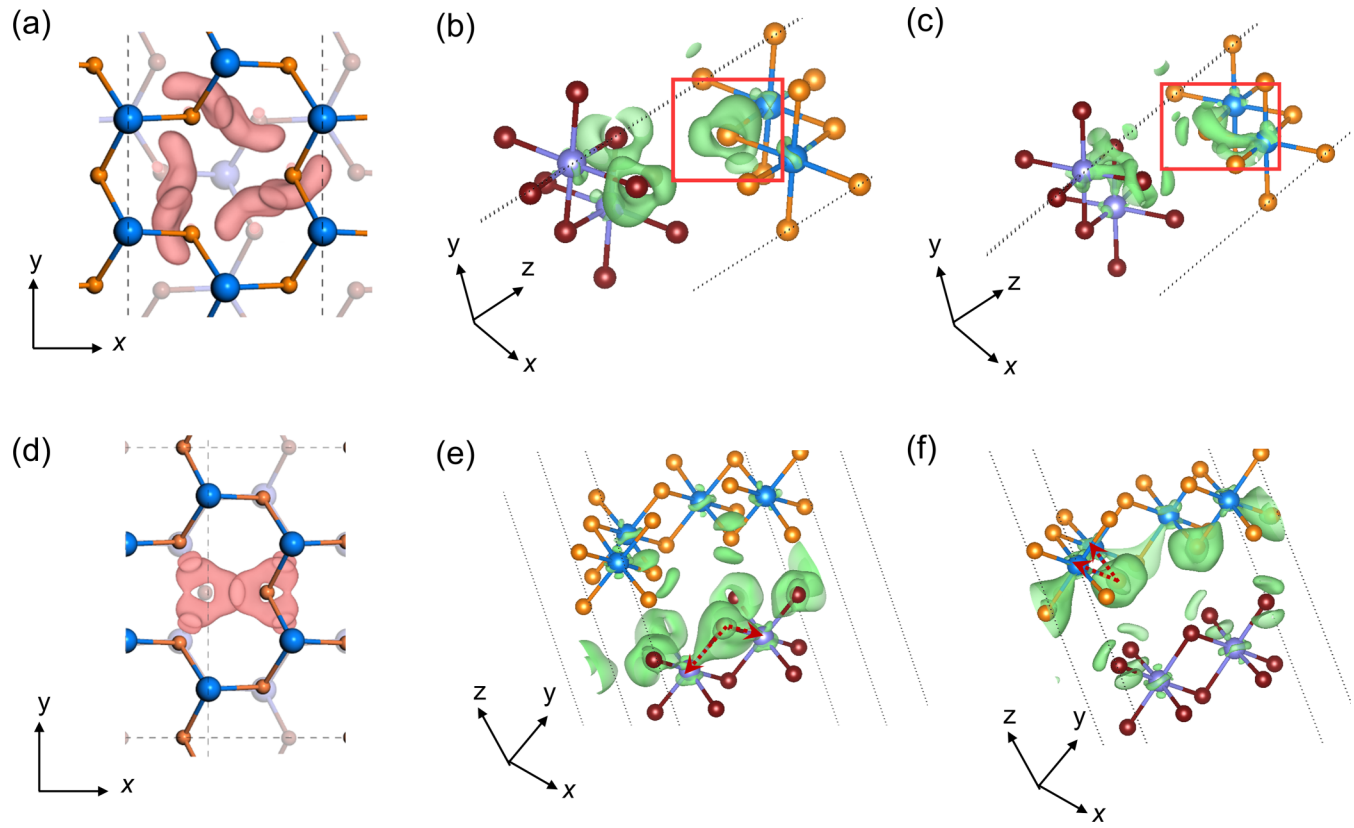

FIG. 9. Spin-dependent differential charge densities in bilayer LT and HT CrI_3. (a)–(c) The total charge accumulation, the charge depletion of spin-up and -down, respectively, in the LT phase. (d)–(f) The respective charge accumulation/depletion in the HT phase. Light-rose and green isosurface indicate charge accumulation and depletion after layer stacking, respectively. The SOC has been considered here.

total magnetization under electric field is smaller than that in Ref. [11], in which it likely results from a combined effect of both electric field and charge doping. Unfortunately, the method combining both effects is under development, which is not directly relevant to the present work.

APPENDIX E: SPIN-DEPENDENT DIFFERENTIAL CHARGE DENSITIES

To illustrate the charge transfer between two layers with different spin component, we calculate the spin dependent differential charge densities as shown in Fig. 9. The charge accumulation for different spin components shares almost the same pattern in LT or HT phases, thus are shown with only one figure for each phase [(a) for the LT phase and (d) for the HT phase], which are also quite similar to that of the total charge shown in Fig. 5. Figures 9(b) and 9(c) show the charge reduction of spin up and down, respectively, in the LT phase. For spin down (c) charge reduction mainly occurs around the $p_{x/y}$ orbitals of I atoms near the interlayer region, indicating a direct FM coupling between the spin-down components (green) of the two I atoms. In the HT case, charge transfer from I atoms forms a triangle-shaped charge accumulation in the interlayer region. Direct charge transfer from the $p_{x/y}$ orbital to the p_z orbital is observable in Figs. 9(e) and 9(f), indicating a direct $p_{x/y}$-p_z interaction.

[1] B. Huang, G. Clark, E. Navarro-Moratalla, D. R. Klein, R. Cheng, K. L. Seyler, D. Zhong, E. Schmidgall, M. A. McGuire, D. H. Cobden, W. Yao, D. Xiao, P. Jarillo-Herrero, and X. Xu, Nature (London) **546**, 270 (2017).

[2] C. Gong, L. Li, Z. Li, H. Ji, A. Stern, Y. Xia, T. Cao, W. Bao, C. Wang, Y. Wang, Z. Q. Qiu, R. J. Cava, S. G. Louie, J. Xia, and X. Zhang, Nature (London) **546**, 265 (2017).

[3] M. Bonilla, S. Kolekar, Y. Ma, H. C. Diaz, V. Kalappattil, R. Das, T. Eggers, H. R. Gutierrez, M.-H. Phan, and M. Batzill, Nat. Nanotech. **13**, 289 (2018).

[4] D. J. O'Hara, T. Zhu, A. H. Trout, A. S. Ahmed, Y. K. Luo, C. H. Lee, M. R. Brenner, S. Rajan, J. A. Gupta, D. W. McComb, and R. K. Kawakami, Nano Lett. **18**, 3125 (2018).

[5] T. Song, X. Cai, M. W.-Y. Tu, X. Zhang, B. Huang, N. P. Wilson, K. L. Seyler, L. Zhu, T. Taniguchi, K. Watanabe, M. A. McGuire, D. H. Cobden, D. Xiao, W. Yao, and X. Xu, Science **360**, 1214 (2018).

[6] D. R. Klein, D. MacNeill, J. L. Lado, D. Soriano, E. Navarro-Moratalla, K. Watanabe, T. Taniguchi, S. Manni, P. Canfield, J. Fernández-Rossier, and P. Jarillo-Herrero, Science **360**, 1218 (2018).

[7] Z. Wang, I. Gutiérrez-Lezama, N. Ubrig, M. Kroner, M. Gibertini, T. Taniguchi, K. Watanabe, A. Imamoğlu, E. Giannini, and A. F. Morpurgo, Nat. Commun. **9**, 2516 (2018).
[8] H. H. Kim, B. Yang, T. Patel, F. Sfigakis, C. Li, S. Tian, H. L. Lei, and A. W. Tsen, Nano Lett. **18**, 4885 (2018).
[9] C. Cardoso, D. Soriano, N. A. Garcia-Martinez, and J. Fernandez-Rossier, Phys. Rev. Lett. **121**, 067701 (2018).
[10] S. Jiang, L. Li, Z. Wang, K. F. Mak, and J. Shan, Nat. Nanotech. **13**, 549 (2018).
[11] S. Jiang, J. Shan, and K. F. Mak, Nat. Mater. **17**, 406 (2018).
[12] B. Huang, G. Clark, D. R. Klein, D. MacNeill, E. Navarro-Moratalla, K. L. Seyler, N. Wilson, M. A. McGuire, D. H. Cobden, D. Xiao, W. Yao, P. Jarillo-Herrero, and X. Xu, Nat. Nanotech. **13**, 544 (2018).
[13] J.-B. Wu, Z.-X. Hu, X. Zhang, W.-P. Han, Y. Lu, W. Shi, X.-F. Qiao, M. Ijias, S. Milana, W. Ji, A. C. Ferrari, and P.-H. Tan, ACS Nano **9**, 7440 (2015).
[14] Y. Cao, V. Fatemi, S. Fang, K. Watanabe, T. Taniguchi, E. Kaxiras, and P. Jarillo-Herrero, Nature (London) **556**, 43 (2018).
[15] T. Jiang, H. Liu, D. Huang, S. Zhang, Y. Li, X. Gong, Y. R. Shen, W. T. Liu, and S. Wu, Nat. Nanotech. **9**, 825 (2014).
[16] J. Hong, C. Wang, H. Liu, X. Ren, J. Chen, G. Wang, J. Jia, M. Xie, C. Jin, W. Ji, J. Yuan, and Z. Zhang, Nano Lett. **17**, 6653 (2017).
[17] H. Wang, F. Fan, S. Zhu, and H. Wu, Europhys. Lett. **114**, 47001 (2016).
[18] P. E. Blöchl, Phys. Rev. B **50**, 17953 (1994).
[19] G. Kresse and J. Furthmüller, Phys. Rev. B **54**, 11169 (1996).
[20] J. Klimes, D. R. Bowler, and A. Michaelides, Phys. Rev. B **83**, 195131 (2011).
[21] J. P. Perdew, K. Burke, and M. Ernzerho, Phys. Rev. Lett. **77**, 3865 (1996).
[22] J. Heyd, G. E. Scuseria, and M. Ernzerhof, J. Chem. Phys. **118**, 8207 (2003).
[23] J. Heyd, G. E. Scuseria, and M. Ernzerhof, J. Chem. Phys. **124**, 219906 (2006).
[24] M. Cococcioni and S. de Gironcoli, Phys. Rev. B **71**, 035105 (2005).
[25] M. A. McGuire, H. Dixit, V. R. Cooper, and B. C. Sales, Chem. Mater. **27**, 612 (2015).
[26] P. Jiang, L. Li, Z. Liao, Y. X. Zhao, and Z. Zhong, Nano Lett. **18**, 3844 (2018).
[27] Y. Zhao, J. Qiao, Z. Yu, P. Yu, K. Xu, S. P. Lau, W. Zhou, Z. Liu, X. Wang, and W. Ji, Adv. Mater. **29**, 1604230 (2017).
[28] J. Qiao, X. Kong, Z. X. Hu, F. Yang, and W. Ji, Nat. Commun. **5**, 4475 (2014).
[29] Y. Zhao, J. Qiao, P. Yu, Z. Hu, Z. Lin, S. P. Lau, Z. Liu, W. Ji, and Y. Chai, Adv. Mater. **28**, 2399 (2016).
[30] Z. X. Hu, X. Kong, J. Qiao, B. Normand, and W. Ji, Nanoscale **8**, 2740 (2016).
[31] J. Qiao, Y. Pan, F. Yang, C. Wang, Y. Chai, and W. Ji, Sci. Bull. **63**, 159 (2018).
[32] C. Wang, X. Zhou, Y. Pan, J. Qiao, X. Kong, C.-C. Kaun, and W. Ji, Phys. Rev. B **97**, 245409 (2018).
[33] K. Liu, L. Zhang, T. Cao, C. Jin, D. Qiu, Q. Zhou, A. Zettl, P. Yang, S. G. Louie, and F. Wang, Nat. Commun. **5**, 4966 (2014).